

Review

Water on Actinide Dioxide Surfaces: A Review of Recent Progress

Gaoxue Wang ¹, Enrique R. Batista ^{2,*} and Ping Yang ^{1,*}¹ T-1, Theoretical Division, Los Alamos National Laboratory, Los Alamos, NM 87545, USA; gaoxuew@lanl.gov² T-CNLS, Theoretical Division, Los Alamos National Laboratory, Los Alamos, NM 87545, USA

* Correspondence: erb@lanl.gov (E.R.B.); pyang@lanl.gov (P.Y.)

Received: 2 June 2020; Accepted: 30 June 2020; Published: 6 July 2020



Abstract: The fluorite structured actinide dioxides (AnO_2), especially UO_2 , are the most common nuclear fuel materials. A comprehensive understanding of their surface chemistry is critical because of its relevance to the safe handling, usage, and storage of nuclear fuels. Because of the ubiquitous nature of water (H_2O), its interaction with AnO_2 has attracted significant attention for its significance in studies of nuclear fuels corrosion and the long-term storage of nuclear wastes. The last few years have seen extensive experimental and theoretical studies on the H_2O – AnO_2 interaction. Herein, we present a brief review of recent advances in this area. We focus on the atomic structures of AnO_2 surfaces, the surface energies, surface oxygen vacancies, their influence on the oxidation states of actinide atoms, and the adsorption and reactions of H_2O on stoichiometric and reduced AnO_2 surfaces. Finally, a summary and outlook of future studies on surface chemistry of AnO_2 are given. We intend for this review to encourage broader interests and further studies on AnO_2 surfaces.

Keywords: actinide dioxide; surface chemistry; water splitting; density functional theory

1. Introduction

The fluorite structured actinide dioxides (AnO_2 , particularly UO_2) are the most common nuclear fuels currently used in nuclear reactors worldwide. Understanding the surface chemistry of these materials is of both fundamental and technological importance owing to its relevance to many aspects in the nuclear industry from the corrosion of nuclear fuels [1,2], hydrogen gas production, and release from nuclear fuels [3], to the handling and long-term storage of spent fuels. As the interaction of nuclear fuels with environmental species (e.g., water and oxygen) starts at their surfaces, there is a pressing need to study the chemical reactions on AnO_2 surfaces to evaluate the environmental impact of spent nuclear wastes [4]. However, the understanding of the surface chemistry of AnO_2 has been severely limited by the difficulties associated with the handling of radioactive actinides in experiments and the complexity of studying actinide systems using theoretical means.

Specialized laboratory equipment is required to handle actinides in experiments, because all the actinide elements are radioactive and very toxic [5,6]. Early actinides such as thorium and uranium are relatively abundant in nature and their most stable isotopes have long radioactive decay times, making them appropriate for laboratory work, for example, the most stable isotopes ^{232}Th and ^{238}U have half-lives of 1.4×10^{10} and 4.5×10^9 years, respectively. The transuranics, on the other hand, are not found in nature and have been artificially made; therefore, they are available in small quantities and are highly radioactive. Therefore, most experimental studies of AnO_2 surface chemistry have focused on UO_2 , leaving the rest of the AnO_2 essentially unexplored. Theoretical calculations can supplement experimental efforts to understand the surface chemistry of the AnO_2 series and some studies have tried to fill this gap. However, the treatment of actinides using electronic structure calculations remains challenging, in comparison with the lighter elements of the periodic table,

owing to a combination of factors: relativistic effects, strongly correlated $5f$ electrons, and noncollinear magnetism. For example, standard exchange-correlation functional of density functional theory (DFT), such as Local Density Approximation (LDA) and Generalized Gradient Approximation (GGA), yields over-delocalized solutions for $5f$ electrons, failing to correctly describe their localization behavior [7,8]. Different approaches have been proposed to circumvent this problem. One of the most popular methods is DFT + U , which involves the introduction of an empirical Hubbard U correction term to the Hamiltonian [9,10]. This method has found high appeal because it does not increase the computational cost and can greatly improve the description of the $5f$ electrons; therefore, it has been widely used to calculate the bulk and surface properties of AnO_2 [7,8,11–16]. However, searching of ground state electronic structure in DFT + U calculations presents additional difficulties [17–20].

Significant experimental and computational efforts have been made to understand the surface chemistry of AnO_2 in the last few years. Herein, we present a brief review of recent progress in the interaction of H_2O with AnO_2 surfaces. We start from the atomic structures of stoichiometric AnO_2 surfaces and their surface energies. Then, the formation of oxygen vacancies and their influence on the oxidation states of actinide atoms are discussed. Finally, we discuss the adsorption and reactions of water on both the stoichiometric and reduced AnO_2 surfaces with oxygen vacancies. This work is not a complete review of all the efforts in the field, but rather we focus on the recent relevant progress in hope that this review can encourage broader interests and further studies on the surface chemistry of AnO_2 .

Bulk AnO_2 from the elements Th through Cf has been observed to crystallize in a fluorite structure, as shown in Figure 1 [6]. In this structure, each actinide atom is eight-fold coordinated, and the oxygen atom is four-fold coordinated. Each actinide atom is formally in the +4 oxidation state, and the oxygen atoms are in the -2 state. The properties of actinide materials are closely dependent on the contraction and stabilization of $5f$ orbitals traversing the actinide series. For example, the lattice constant of bulk AnO_2 shows a monotonic decrease from ThO_2 to CfO_2 , however, it deviates from the trend at CmO_2 as a result of orbital mixing and covalency between the metal $5f$ and the oxygen $2p$ orbitals. This increased orbital mixing can be tracked down to the proximity in energy between those two orbital manifolds and is now referred to as energy-driven covalency in the literature [21].

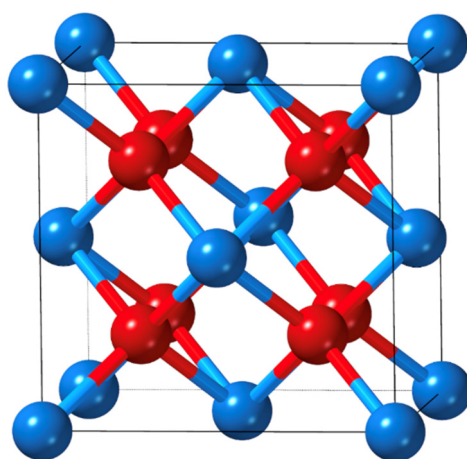


Figure 1. Unit cell of fluorite AnO_2 . The blue and red atoms correspond to the actinide and oxygen atoms, respectively.

The surface properties (surface energy, reconstruction, reactivity, and so on) of AnO_2 are highly dependent on the surface geometry. The top and side views of the low indexed (111), (110), and (100) surfaces of AnO_2 are shown in Figure 2. Along the (111) direction, the surface consists of alternating oxygen and actinide layers with a tri-layer structure (O-An-O). Each tri-layer has a net dipole moment of zero in the direction perpendicular to the surface [22], and the most stable surface is terminated by an oxygen layer. Along the (110) direction, a series of neutral AnO_2 planes are found; therefore,

the surface is nonpolar. Along the (100) direction, AnO_2 consists of alternating oxygen and actinide layers with the sequence of $-\text{O}_2-\text{An}-\text{O}_2-\text{An}-\text{O}_2-$. Cleaving the crystal perpendicular to the (100) direction yields a polar surface with a net dipole moment, which is inherently unstable. A nonpolar stable surface is achieved by the removal of half of the oxygen atoms from the surface. This reconstruction leads to a slab-type unit cell of the form $\text{O}-\text{An}-\text{O}_2-(\text{An}-\text{O}_2)_n-\text{An}-\text{O}_2-\text{An}-\text{O}$, as shown in Figure 2. The surface that contains 50% oxygen vacancies on the topmost oxygen layer has been observed for UO_2 (100) [23,24].

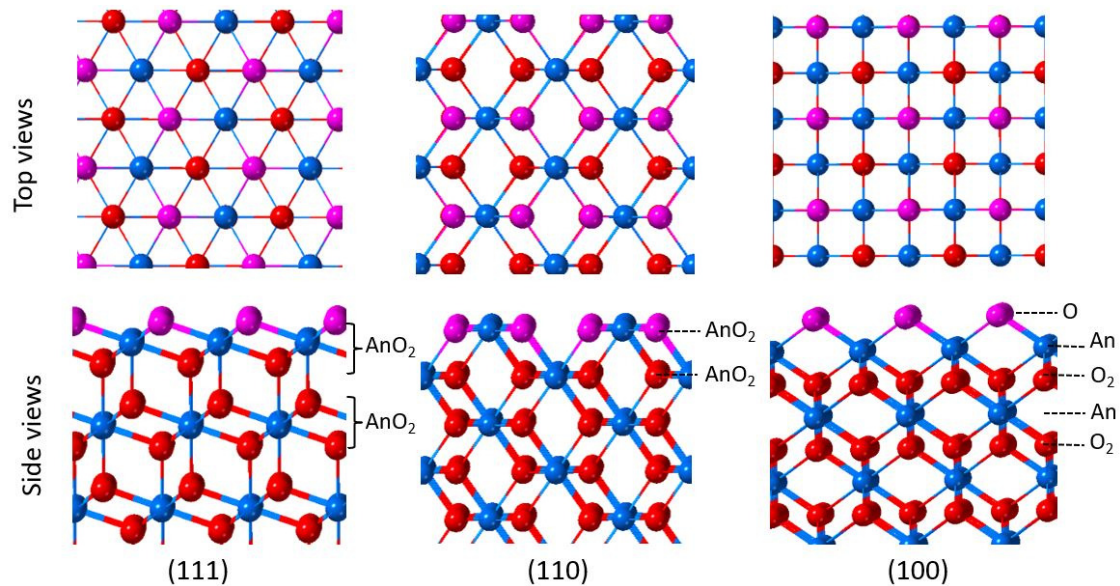


Figure 2. Top and side views of the (111), (110), and (100) surfaces of AnO_2 .

Calculated surface energies of AnO_2 have been reported in several papers, particularly for ThO_2 , UO_2 , and PuO_2 . Tables 1–3 summarize the surface energies for the low indexed (111), (110), and (100) surfaces, comparing the different reports that employed DFT and those that relied on other classical models [25–33]. It is seen that DFT calculations give rise to smaller surface energies than the classical models for ThO_2 , UO_2 , and PuO_2 surfaces. A variation in the surface energies is also observed for DFT calculations owing to the use of different level of theory and parameters in the calculations. Despite the variation in the calculated surface energies, all these calculations predict the (111) surface to have the lowest surface energy, hence being the most stable surface for AnO_2 . Therefore, nanocrystals of AnO_2 are expected to be mostly terminated by the (111) surface and grow in octahedral shape, according to the Wulff constructions [34]. The relative stability of surfaces can be modified through the selective adsorption of organic ligands on different surfaces, which is key for the controlled synthesis of nanocrystals with different morphologies [35,36].

Table 1. ThO_2 surface energies in units of J/m^2 . DFT, density functional theory.

References	Methods	$\gamma_{(111)}$	$\gamma_{(110)}$	$\gamma_{(100)}$	
Rak et al. [37]	GGA + U ($U = 4 \text{ eV}$)	0.79	1.18	-	
Alexandrov et al. [38]	DFT	GGA	0.8	1.10	1.6
Skomurski et al. [2]		GGA	0.72–0.81	0.98–1.30	1.55–1.75
Shields et al. [39]		GGA	0.50	0.75	1.30
Wang et al. [35]		GGA	0.801	1.202	1.762
Tasker et al. [25]	Classical models	Ionic shell model	1.016	1.451	-
Chatzimichail et al. [26]		Thermodynamic model	0.973	1.297	1.382

Table 2. UO₂ surface energies in units of J/m².

References	Methods	$\gamma_{(111)}$	$\gamma_{(110)}$	$\gamma_{(100)}$
Skomurski et al. [2]	GGA	0.59–0.33	1.01–0.83	1.21–1.07
Rak et al. [37]	GGA + <i>U</i> (<i>U</i> = 4 eV)	0.78	1.05	1.47
Evarestov et al. [40]	Hybrid functional	0.94	-	-
Chaka et al. [41]	GGA	0.888	-	-
Weck et al. [42]	GGA + <i>U</i> (<i>U</i> = 0 to 4 eV)	0.76–0.78	-	-
Bo et al. [22]	GGA + <i>U</i> (<i>U</i> = 4 eV)	0.71	1.08	1.49
Bottin et al. [43]	GGA + <i>U</i> (<i>U</i> = 4 eV)	0.73	1.16	1.46
Rabone et al. [20]	GGA + <i>U</i> (<i>U</i> = 3.96 eV)	0.48	0.77	1.25
Tasker et al. [25]	Ionic shell model	1.064	1.561	-
Abramowski et al. [27]	Born model	1.27	2.0	2.72
Tan et al. [29]	Pair potentials	1.29	2.04	2.45
Jelea et al. [30]	Ionic crystal interatomic potentials	1.24	-	2.22
Sattonay et al. [31]	Tight-binding variable-charge model	1.07	1.72	2.03
Benson et al. [32]	Born–Mayer model	1.030	-	-
Chatzimichail et al. [26]	Thermodynamic model	0.95	1.266	1.333
Boyarchenkov et al. [33]	Pair potentials	1.14	-	1.60

Table 3. PuO₂ surface energies in units of J/m².

References	Methods	$\gamma_{(111)}$	$\gamma_{(110)}$	$\gamma_{(100)}$
Sun et al. [44]	LDA/GGA + <i>U</i> (<i>U</i> = 4 eV)	0.72–1.04	1.20–1.44	1.52–1.84
Jomard et al. [28]	GGA + <i>U</i> (<i>U</i> = 3.3 eV)	0.72–0.74	1.10–1.13	1.64–1.69
Rak et al. [37]	GGA + <i>U</i> (<i>U</i> = 4 eV)	0.74	1.15	1.76

2. Oxygen Vacancies on AnO₂ Surfaces

The effect of oxygen vacancies is crucial for understanding the reactivity of AnO₂ surfaces as radiation damage can lead to the formation of vacancies on these surfaces. Indeed, studies of the reactivity of H₂O on UO₂ surfaces indicate weak reactivity on stoichiometric UO₂ (111) surface, while dissociative adsorption and hydrogen (H₂) formation upon reduction of the surfaces with oxygen vacancies [45,46]. Similarly, oxygen vacancies have been demonstrated to have a strong impact on the surface chemistry of transition metal and lanthanide oxides, as evidenced by the catalytic properties of CeO₂, a close sibling of AnO₂ sharing the crystal structure and oxidation states [38]. The formation of an oxygen vacancy in CeO₂ leaves two excess electrons in the host material, which localize at two 4*f* orbitals of Ce sites, reducing them to Ce³⁺ [47]. The formation of Ce³⁺ has been demonstrated to alter the reactivity of CeO₂ (111) surface, such as the activation of the acetaldehyde for coupling reactions [48]. The integrated experimental and theoretical efforts have made great progress in understanding its surface reactivity and reaction mechanism. In this section, we will illustrate the progress for the AnO₂ systems.

2.1. Experimental Work

A thorough experimental study of oxygen vacancies on AnO_2 surfaces has only been performed on UO_2 (111) surface. Artificial oxygen vacancies on UO_2 (111) surfaces were created using Ar^+ sputtering, and the oxidation states of surface actinide atoms were studied using X-ray photoelectron spectroscopy (XPS) [45]. A comprehensive review of XPS spectra of uranium oxide powder, thin films, and single crystals can be found in the work of [49]. Figure 4 shows the XPS spectra of stoichiometric UO_2 (111) surface (A), the surface after Ar^+ sputtering at 300 K (B), and after Ar^+ sputtering at 90 K (C) [45]. The stoichiometric surface has the $\text{U}4f^{7/2}$ and $\text{U}4f^{5/2}$ peaks at 380.0 and 390.8 eV, and two characteristic satellite peaks S^1 and S^2 at 386.7 and 397.3 eV [45]. Similar peak positions have been reported in various studies for the U^{4+} , suggesting that uranium atoms on the stoichiometric surface remain in U^{4+} as in the bulk UO_2 [50,51]. After sputtering with Ar^+ at 300 K, a shoulder on the lower binding energy side of the $4f$ peaks appears. The broad shoulder has been attributed to uranium atoms in different oxidation states from +4 to 0 (uranium metal) and the slight shift of the $\text{U}4f^{7/2}$ and $\text{U}4f^{5/2}$ is owing to the formation of an n -type semiconductor upon the creation of oxygen vacancies [45]. The formation of different oxidation states of uranium atoms on the surfaces with oxygen vacancies is evidenced in the fit of XPS spectra, as shown in Figure 3 [49]. An improved fit of the shoulder of $\text{U}4f^{7/2}$ peak can be obtained via the inclusion of peaks corresponding to the different oxidation states between +4 and 0, indicating the presence of uranium atoms in the reduced states [49]. However, deriving the structure of an oxygen vacancy at the atomic layer of UO_2 surface and its electronic properties from these XPS data is still not possible without the complementation of DFT simulations. This is because most of the surface analysis techniques such as XPS and Auger electron spectroscopy (AES) have a penetration depth of a few nanometers [52], thus the signal from XPS and AES typically represents an average over a few nanometers of the materials.

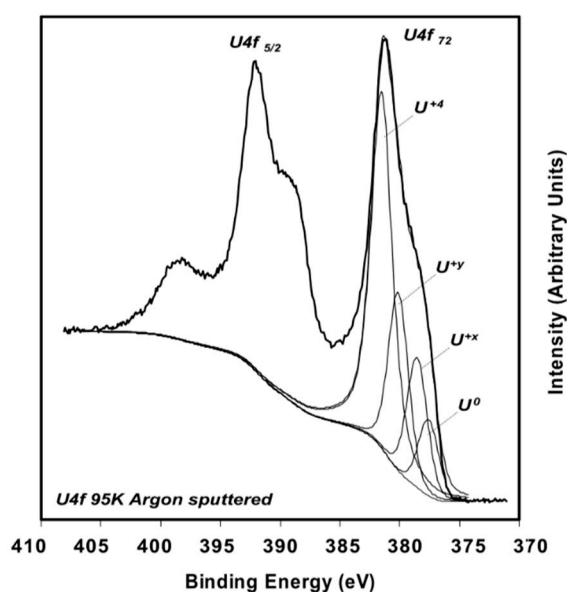


Figure 3. XPS spectra of reduced UO_2 (111) surface [49]. The broad shoulder of $\text{U}4f^{7/2}$ peak can be better fitted by considering different oxidation states of uranium from +4 to 0.

2.2. Theoretical Calculations

Several DFT simulations have been reported on the study of oxygen vacancies on the top-surface and the subsurface of AnO_2 , providing insights in terms of the electronic structure of the reduced surfaces, the oxidation states of actinide atoms, the formation energies of vacancies, and the electronic structure of excess electrons owing to oxygen vacancies.

Table 4 shows the calculated formation energies of oxygen vacancies on (111) surface of ThO₂, UO₂ and PuO₂. The formation energy is defined as $E_v = E_{slab} - (E_{v,slab} + \frac{1}{2}E_{O_2})$, where $E_{v,slab}$ and E_{slab} are the total energy of the slab with and without oxygen vacancy, respectively. E_{O_2} is the total energy of one isolated O₂ molecule in its ground state. From these calculations, it is seen that the oxygen vacancy formation energies decrease from ThO₂ to PuO₂ [44,53–55]. Recent studies found that the oxygen vacancy formation energies are correlated with the reduction potential of An⁴⁺, in accordance with the *f*-band energy drops as going down the actinide series [53,56]. Interestingly, the fundamental question regarding the relative stability of oxygen vacancy in the top-surface and subsurface is still debatable, although similar DFT + *U* calculations were used [53,54]. The conclusions for PuO₂ (111) surface are consistent that the oxygen vacancy formation energy is slightly lower in the top-surface than in the subsurface in previous studies [44,53], and the energy difference is within 0.05 eV. However, it has been demonstrated that oxygen vacancy in the subsurface is more stable than in the top-surface on CeO₂ (111) surface, which has an identical structure to AnO₂ [47]. Besides the debate of the relative stability of oxygen vacancy in the top-surface and subsurface of AnO₂, inconsistent results about the distribution of the excess electrons were also reported. On the UO₂ (110) surface, some theoretical calculations based on Perdew-Burke-Ernzerhof (PBE) functional and an effective Hubbard *U* value of 4.0 eV found that the excess electrons are localized on two uranium atoms, resulting in two U³⁺ next to the vacancy site [54]. Other theoretical studies reported the two electrons to be delocalized over three uranium atoms by natural population analysis for the embedded cluster calculations [53].

Table 4. Formation energies of top-surface and subsurface oxygen vacancy in AnO₂ (111) surfaces.

In Units of eV		ThO ₂	UO ₂	PuO ₂
Wellington et al. [53]	Top	-	6.45	3.35
	Sub	-	6.14	3.40
Bo et al. [54]	Top	-	5.95	-
	Sub	-	6.08	-
Sun et al. [44]	Top	-	-	2.85
	Sub	-	-	2.89
Wang et al. [55]	Top	6.95	5.21	2.81
	Sub	6.58	4.98	2.43

The inclusion of a Hubbard-like on-site Coulomb interaction in DFT + *U* yields a more accurate treatment of the correlated electrons, which overcomes deficiencies of the pure LDA/GGA functionals and has achieved a wide range of successes in treating AnO₂ [7,8]. However, the inclusion of Hubbard term introduces multiple energy local minima, which complicates the search for the ground state [17–20]. Several methods, such as *U*-ramping [19] and occupation matrix control (OMC) [17,18], have been proposed to overcome this difficulty presented by DFT + *U*. These methods have been shown to locate low-energy solutions for a variety of systems containing strongly correlated *d* and *f* electrons [17–19]. Recently, these approaches have been applied to the study of reduced AnO₂ (111) surfaces [55]. It was found for ThO₂, UO₂, and PuO₂ (111) surfaces that the oxygen formation energy is 0.23–0.38 eV lower for the subsurface vacancy. This is consistent with the calculations for CeO₂ (111) surface, where explicit searching of the low-energy solutions has been carried out by assigning excess electrons to different sites near the vacancy [47,57]. The unexpected lower formation energy for oxygen vacancy energy in the subsurface has been explained in terms of smaller Madelung potential owing to defect-induced lattice relaxation [47]. The excess electrons on the ThO₂ surface stay at the vacancy site, forming a lone electron pair, as shown in Figure 5a,b. On the UO₂ surface, one of the excess electrons stays at the vacancy site, and the other moves to uranium 5*f* orbitals, reducing it to U³⁺ (Figure 5c,d). On the PuO₂ surface, both excess electrons localize at the Pu 5*f* orbitals reducing two next-nearest Pu sites

(Figure 5e,f). More advanced experimental surface-sensitive characterization will be needed in order to settle the debate and validate these predicted theoretical results.

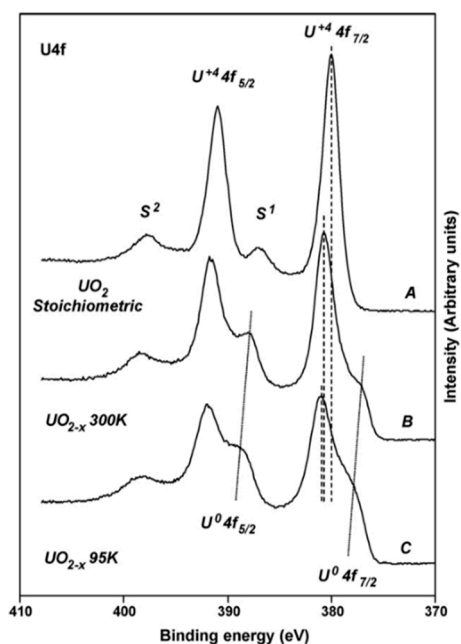


Figure 4. X-ray photoelectron spectroscopy (XPS) spectra of stoichiometric UO_2 (111) surface and the surface after sputtering with Ar^+ [45].

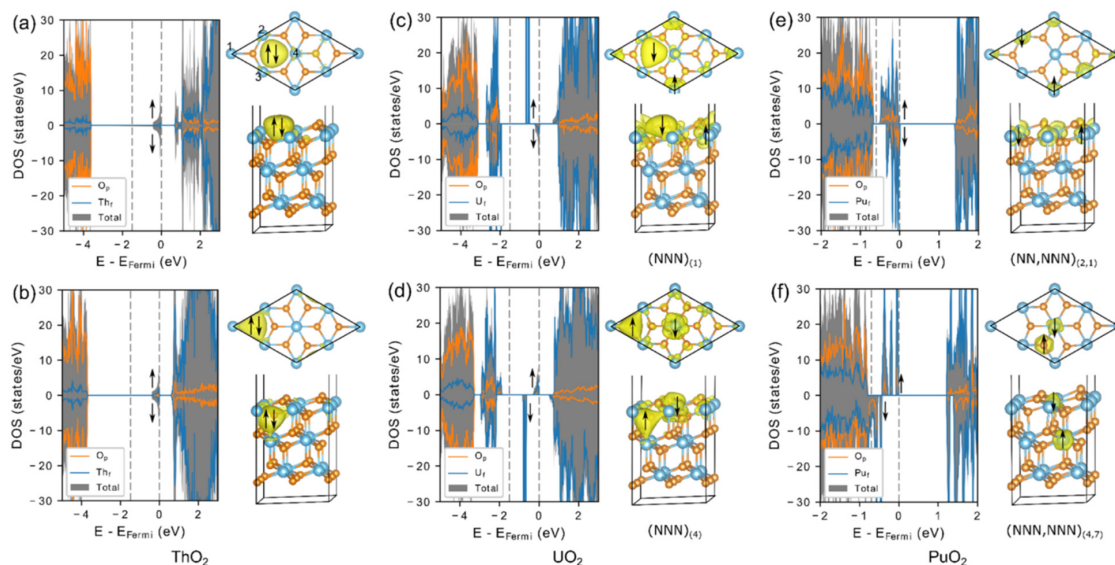


Figure 5. Density of states (DOS) and partial charge density plots of reduced ThO_2 , UO_2 , and PuO_2 (111) surfaces with oxygen vacancy in the top-surface (a,c,e) and in the subsurface (b,d,f) [55].

3. Water on AnO_2 Surfaces

The interaction of water with AnO_2 has attracted numerous works owing to its importance for the storage of nuclear fuels [1,2,4]. In particular, the adsorption, dissociation, and reaction pathways of water on UO_2 and PuO_2 surfaces have been of great interest. For UO_2 , the interaction of water with both perfect and reduced single crystalline (111) films and polycrystalline films has been carried out [58,59]. On PuO_2 surfaces, several experimental studies have been performed on polycrystalline films [1,60–63].

3.1. Experiments

The interaction of H₂O with AnO₂ surfaces initiates with its adsorption and dissociation on the surfaces. It has been shown that the adsorption of H₂O molecules on UO₂ (111) surface is reversible (80%) at 300 K, indicating that H₂O is weakly adsorbed on perfect UO₂ (111) surface [58]. On the contrary, H₂O is strongly adsorbed on surfaces with oxygen vacancies. Figure 6 shows the XPS spectra of reduced surface after exposure to heavy water (D₂O), then followed by annealing at different temperatures [45]. It is clearly seen that the shoulders for the U4f ^{7/2} peaks disappear after exposure to D₂O and subsequent annealing. This implies the recovery of uranium atoms to the formal oxidation state of +4. More interestingly, temperature programmed desorption (TPD) experiments for H₂ release upon exposing water to an Ar⁺ sputtered UO₂ surface show that H₂ production can only occur on reduced (111) surface with oxygen vacancies (Figure 7). The amount of H₂ desorption increases with the Ar⁺ sputtering time, namely the concentration of oxygen vacancies on the surfaces [58]. These experiments demonstrate that the interaction of H₂O with AnO₂ surfaces is dependent on the surface oxygen vacancies, and oxygen vacancies prompt the dissociation of H₂O and the production of H₂ on AnO₂ surfaces. The interaction of H₂O with PuO₂ films has been studied using XPS and ultra-violet photoelectron spectroscopies (UPS) [60,61]. It was found that H₂O dissociates and forms a thin hydroxyl (OH⁻) layer with small amounts of molecularly adsorbed water at 298 K. While under 80–120 K, H₂O is adsorbed as thick ice multilayers and no significant OH⁻ is detected. The top surface layer can be reduced to Pu₂O₃ when the ice covered PuO₂ is warmed up under ultraviolet light, while the mechanism of the reduction is still unclear [61]. Another study has reported that H₂O can catalyze the oxidation of PuO₂ surfaces and the formation of stable compounds PuO_{2+x} (x ≤ 0.27) containing Pu⁶⁺ [1].

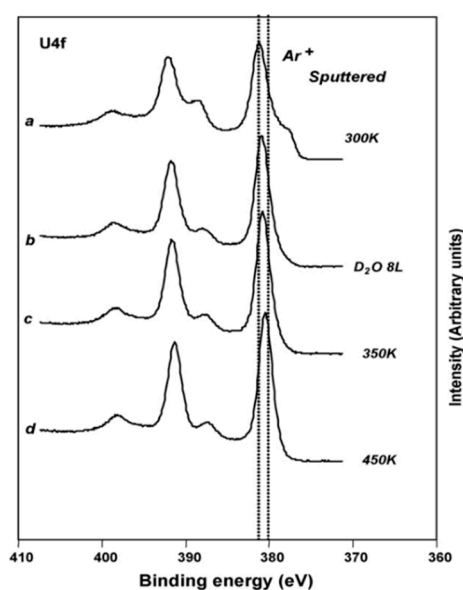


Figure 6. XPS spectra of reduced UO₂ (111) surface after exposure to D₂O [45].

3.2. Theoretical Calculations

Contrary to the lack of experimental data, several theoretical groups have pioneered modeling of H₂O on stoichiometric and reduced AnO₂ surfaces [22,44,53,54,64]. These simulations shed light on the nature of the fundamental interaction between H₂O and AnO₂ surfaces. We will discuss these advances in two main aspects: (i) adsorption and dissociation of water and (ii) mechanism of H₂ production.

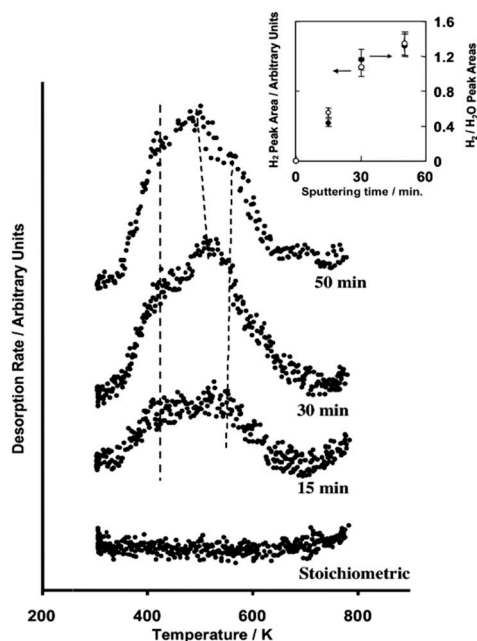


Figure 7. Temperature programmed desorption of H_2 after H_2O adsorption at 300 K over Ar^+ sputtered UO_2 (111) single crystal [58]. The inset shows the computed H_2 peak area as well as the H_2/H_2O peak area ratios.

3.2.1. Adsorption and dissociation of H_2O on AnO_2 surfaces

The adsorption and dissociation of H_2O on AnO_2 surfaces have been extensively studied in several papers [44,53,54,64,65]. H_2O molecules can adsorb on surfaces in the molecular form or the dissociated form. For the molecular adsorption (Figure 8a,b), the oxygen atom from the H_2O molecule binds via its lone pair with the positive actinide atom on the surface, while, at the same time, one of the hydrogen atoms forms a hydrogen bond with a nearby oxygen atom on the surface. If the H_2O dissociates at the surface into OH^- and H^+ , the hydroxyl group bonds with one surface actinide atom, and the proton bonds with one surface oxygen atom (Figure 8c,d). On the basis of these studies [44,53,54,64], the following general conclusions have been reached on the adsorption and dissociation of H_2O on AnO_2 surfaces:

- (i) A mixture of molecular and dissociative adsorption of H_2O occurs on the (111) surface of AnO_2 .
- (ii) Dissociative adsorption of H_2O preferentially occurs on the (110) and (100) surfaces of AnO_2 .
- (iii) The adsorption energies of H_2O are correlated with the surface energies; a stronger adsorption energy is expected on the surface with a higher surface energy.
- (iv) The presence of oxygen vacancies on the surface of AnO_2 favors the dissociative adsorption mechanism. The distribution of excess electrons on reduced AnO_2 surfaces is different upon the adsorption of H_2O .

Alexandrov et al. first studied the adsorption configurations of H_2O on ThO_2 surfaces using both accurate calorimetric measurements and first-principle calculations [38]. They observed coverage-dependent adsorption energies and demonstrated a mixture of molecular and dissociative adsorption of H_2O on ThO_2 (111) surface. They also showed that the adsorption energy of water molecules is correlated with the surface energies; a higher surface energy results in a stronger water adsorption on ThO_2 surfaces [38]. Bo et al. [22] found that, for a single water molecule on UO_2 (111) surface, the two adsorption configurations, molecular adsorption and dissociative adsorption, exhibit comparable adsorption energies (0.61 vs. 0.68 eV, as shown in Table 5). However, the adsorption in the molecular form, on (110) and (100) surfaces, is far less stable than the dissociative adsorption (0.62 vs. 1.27 eV and 1.02 vs. 1.71 eV, respectively) [22]. Bo's results are consistent with those of

Wellington et al. [66] and Tegner et al. [67], who also found that the molecular and dissociative adsorptions have similar adsorption energies on UO_2 and PuO_2 (111) surfaces, while there is a clear preference for dissociative adsorption on (110) surfaces. Both groups reported the mixture of molecular and dissociative adsorption to be the most stable adsorption configuration at a higher coverage of H_2O on (111) surfaces [22,66,67]. The calculated adsorption energies of H_2O on UO_2 surfaces increase from (111), (110), to (100) surface, as summarized in Table 5, which is consistent with the observation by Alexandrov et al. that stronger H_2O adsorption energies are expected on ThO_2 surfaces with higher surface energies [38]. Tegner et al. further studied the adsorption of up to five layers of H_2O on PuO_2 and UO_2 surfaces, and found significant variation in the adsorption energies as a result of intra- and interlayer hydrogen bonding network [68].

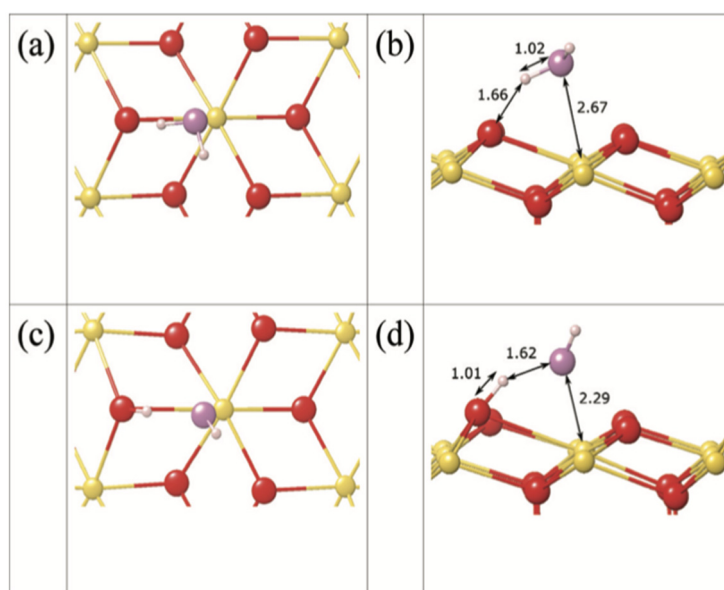


Figure 8. H_2O on ThO_2 (111) surface [38]. Top and side views of molecular adsorption (a,b) and dissociative adsorption (c,d).

Table 5. Adsorption energies of one H_2O molecule on perfect UO_2 surfaces. The bold italic numbers correspond to adsorption energies in the dissociative form. The rest are adsorption energies in the molecular form.

In Units of eV	(111)	(110)	(100)
Bo et al. [22,54]	0.61 <i>0.68</i>	0.62 <i>1.27</i>	1.02 <i>1.71</i>
Tegner et al. [67]	0.53 <i>0.50</i>	0.93 <i>1.39</i>	0.97 <i>1.55</i>
Wang et al. [55]	0.62	-	-

Ab-initio molecular dynamics (AIMD) simulations have also been carried out to explore the mechanism of adsorption and dissociation of H_2O on AnO_2 surfaces. It was found that the dissociative adsorption of H_2O is feasible for a large range of temperature and water partial pressures on UO_2 (111) surface [69]. The dissociation of H_2O on PuO_2 (110) surface is a two-step hydroxylation process both for single H_2O molecule and H_2O clusters [70]. The dissociation is initiated by the dehydrogenation of water molecules to form a hydroxyl group with surface oxygen atom, followed by successive surface hydroxylation on plutonium with the remaining hydroxide ion of the dissociating molecule. The H_2O molecule dissociates as the consequence of hybridizations between the molecular orbitals of water and

the electronic state of the surface with a reaction energy barrier of 0.18 eV. In contrast, the dissociation of H₂O clusters is exothermic by −0.42 eV with no energy barrier [70].

On reduced AnO₂ surfaces with oxygen vacancies, H₂O has much stronger adsorption energies, as shown in Table 6. On perfect ThO₂, UO₂, and PuO₂ (111) surfaces, the adsorption energy of water is smaller than 1.1 eV from DFT calculations [38,54,55,64,67], while the adsorption energies are larger than 1.8 eV on surfaces with oxygen vacancies [53–55,64]. These DFT calculations are in agreement with experimental results by Senanayake et al. that the adsorption of H₂O on UO₂ (111) surface is weak and reversible (80%) at 300 K [58]. DFT simulations also found that the dissociation of H₂O on reduced AnO₂ surfaces can occur spontaneously at room temperature, as there is a very small energy barrier for the dissociation [54,55]. After H₂O dissociation, the hydroxylate group moves to the oxygen vacancy site, and the proton binds with one surface oxygen atom as shown in Figure 9. The excess electrons are distributed differently on reduced AnO₂ surfaces upon the adsorption of H₂O. On reduced ThO₂ (111) surface, the excess electrons still stay at the vacancy site after H₂O dissociation. One proton from the H₂O molecule is attracted to the vacancy site and forming H⁺. However, on both reduced surfaces, UO₂ and PuO₂ (111), the OH[−] group from H₂O tends to fill the vacancy site. When OH[−] moves to the vacancy site for UO₂ surface, it will push the excess electron to a neighboring uranium site and reduce it to U³⁺.

3.2.2. H₂ production from H₂O splitting

The formation of H₂ owing to the interaction of H₂O with AnO₂ through radiolytic process or chemical reactions can lead to potential pressurization of the containers of nuclear fuels. The formation of H₂ on AnO₂ surfaces owing to chemical reactions with H₂O has rarely been studied in theoretical calculations [54,55]. Bo et al. first systematically investigated the formation and desorption mechanism of H₂ on reduced UO₂ (111) surface [54]. They found that H₂ formation can occur on UO₂ (111) surface with the oxygen vacancies [54]. Figure 10 shows the three possible reaction pathways [54]. The first formation pathway in Figure 10a involves the direct dissociation of H₂O at a vacancy site, forming O-H-H structure on the surface, followed by the desorption of H₂ from the surface and oxygen atom healing the vacancy. This pathway has an energy barrier of 0.56 eV, and the overall reaction is exothermic by 2.62 eV [54]. The second pathway in Figure 10b involves the dissociation of H₂O on the surface, forming hydroxylated surface, and then the combination of the hydrogen atoms from the hydroxyl radicals to form H₂ molecules. This pathway presents a large energy barrier of 1.39 eV and an overall exothermic energy of 2.56 eV. For the third pathway in Figure 10c, there are excess hydroxyl radicals near the vacancy site. The dissociation of H₂O will result in a hydroxyl radical that occupies the vacancy site, and the formation of O-H-H structure. This reaction pathway is also exothermic by 1.98 eV and has an energy barrier of 0.53 eV [54].

A comparative study of H₂ formation on reduced ThO₂, UO₂, and PuO₂ (111) surfaces has been performed to show the difference in the H₂ formation across the AnO₂ series [55]. It is found that the formation of H₂ from catalytic splitting of H₂O is endothermic for all three AnO₂ (111) surfaces evaluated (Table 7). In contrast, H₂O can readily dissociate on the reduced ThO₂, UO₂, and PuO₂ (111) surfaces, while the thermodynamics of H₂ production is significantly different [55]. On reduced ThO₂ (111) and UO₂ (111) surfaces, the H₂O adsorption and H₂ production is exothermic and releases 3.55 eV and 3.11 eV, respectively (Table 7). Although this process releases 0.31 eV on reduced PuO₂ (111) surface, there is a larger energy barrier for the H₂ production. This suggests that the protons of H₂O will stay in the hydroxylated form on PuO₂ (111) surface, instead of forming H₂ molecule [55]. The high reactivity of H₂O with reduced ThO₂ surface is attributed to the lone electron pair at the vacancy site on ThO₂ that can readily participate in the chemical reactions with H₂O. On the contrary, the excess electrons are more tightly bound to the Pu 5*f* orbitals on reduced PuO₂ surfaces, thus making it harder to participate in the reaction with H₂O molecule.

Table 6. Adsorption energies of one H₂O molecule on AnO₂ (111) surface. The bold italic numbers correspond to the dissociative adsorption energies. The rest are the molecular adsorption energies.

In Units of eV	Perfect			Reduced		
	ThO ₂	UO ₂	PuO ₂	ThO ₂	UO ₂	PuO ₂
Tegner et al. [67]	-	0.53 <i>0.50</i>	0.40 <i>0.32</i>	-	-	-
Wellington et al. [53]	-	-	-	-	2.23	2.10
Bo et al. [54]	-	0.61 <i>0.68</i>	-	-	2.20	-
Alexandrov et al. [38]	0.57 <i>0.67</i>	-	-	-	-	-
Tian et al. [64]	-	1.08 <i>0.68</i>	-	-	1.88	-
Weck et al. [42]	-	0.85 <i>0.60</i>	-	-	-	-
Wang et al. [55]	0.56	0.62	0.58	2.63	1.90	2.44

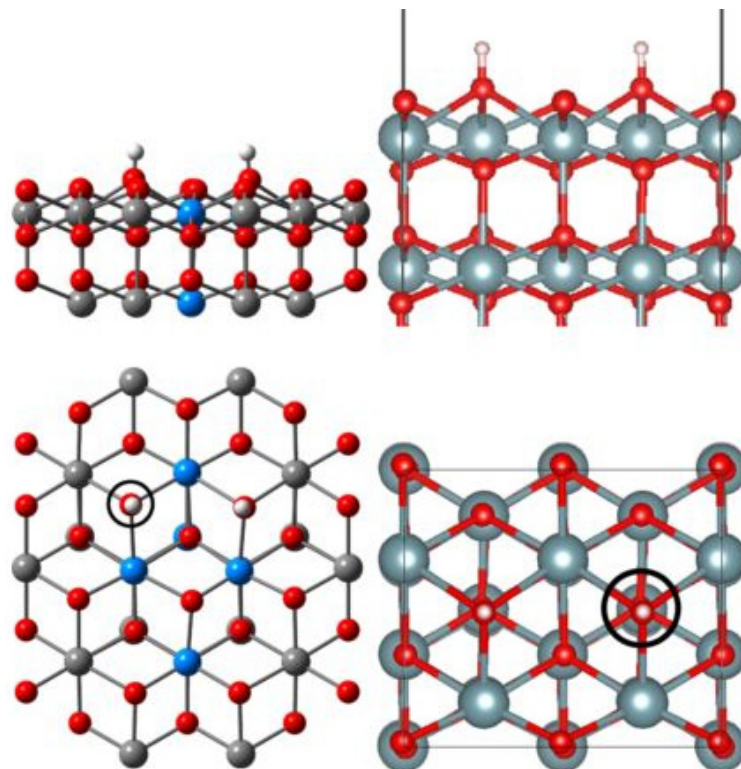


Figure 9. Dissociative adsorption of H₂O molecule on UO₂ (111) surface with oxygen vacancy [53]. The left is the side and top views using the embedded cluster model, the right is using the periodic model. The position of the oxygen vacancy is indicated with a black circle.

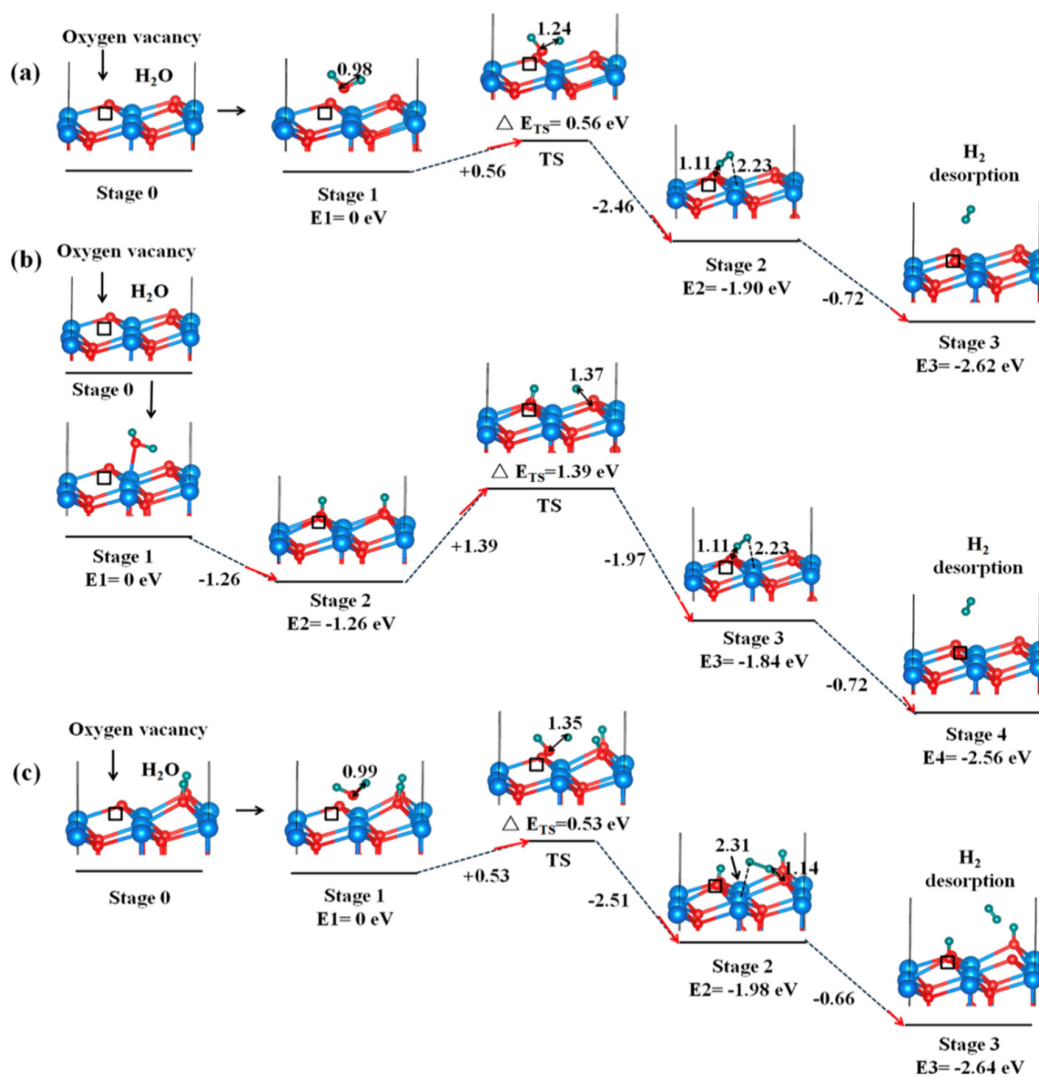


Figure 10. H₂O dissociation and H₂ production on reduced UO₂ (111) surface through three different reaction pathways (a–c) [54].

Table 7. The reaction energy of H₂O splitting and H₂ formation (H₂O → O* + H₂) on perfect ThO₂, UO₂, and PuO₂ (111) surfaces and corresponding surfaces with oxygen vacancies. A negative/positive value represents the reaction is exothermic/endothermic, respectively.

ΔH (eV)	ThO ₂	UO ₂	PuO ₂
Perfect surface	+1.72	+1.85	+4.11
Oxygen vacancy	−3.55	−3.11	−0.31

4. Summary and Outlook

Understanding the surface chemistry of AnO₂ is relevant to many stages in the nuclear industry. Significant efforts have been performed in the community to explore the interaction of H₂O with AnO₂ surfaces. These studies provide significant insights on the adsorption and dissociation of H₂O, the vacancy formation, and the H₂ production on the AnO₂ surfaces owing to chemical reactions with H₂O. There is still important work to be done in this area. (i) AnO₂ surfaces beyond UO₂: Previous experimental studies mostly focus on UO₂ surfaces. The rest of the AnO₂ surfaces have been hardly explored in experiments. Especially, controlled synthesis of high quality AnO₂ films using advanced techniques, such as polymer assisted deposition (PAD), atomic vapor deposition, and crystal

truncation rod (CTR), among others, is needed to study the surface chemistry of AnO₂ surfaces beyond UO₂. (ii) AnO₂ surfaces with complicated surface structures: Compared with experiments that mostly focus on UO₂ films, more theoretical simulations have been conducted on AnO₂ surfaces beyond UO₂. However, most of the simulations are on low indexed (111), (110), and (100) surfaces of AnO₂, because the simulation cells are smaller and more accessible to computational methods than the high indexed ones. In fact, other surfaces with higher surface energy are expected to be more reactive, which might be more important for understanding the dissolution, reactivity, and environmental effects of nuclear fuels. Moreover, defected surfaces with only one oxygen vacancy have been investigated in earlier work, while defected surfaces with more complicated structures are yet to be explored both in experiments and in theory. (iii) Chemical reactions on the surfaces and reaction dynamics. Previous theoretical simulations are limited to small systems with a few water molecules on the surfaces and the very early stage of H₂O interaction with the surfaces owing to the computational cost of DFT simulations. To this regard, developing methods that can deal with large systems and perform dynamics on a long time scale, such as density functional tight binding (DFTB) [71], is in urgent need to study the AnO₂ surfaces, chemical reactions and dynamics on the surfaces, and their interactions with the environments.

Author Contributions: Writing—original draft preparation, G.W.; writing—review and editing, E.R.B. and P.Y.; supervision, E.R.B. and P.Y.; All authors have read and agreed to the published version of the manuscript.

Funding: This research was funded by Laboratory Directed Research and Development program of Los Alamos National Laboratory (LANL), grant number 20160604ECR, 20180007DR, and US DOE office of Basic Energy Science under the Heavy Element Chemistry program.

Acknowledgments: G.X.W. acknowledges the Director's Postdoc Fellow from LANL. LANL, an affirmative action/equal opportunity employer, is managed by Triad National Security, LLC, for the National Nuclear Security Administration of the U.S. Department of Energy under Contract 89233218CNA000001.

Conflicts of Interest: The authors declare no conflict of interest.

References

1. Haschke, J.M.; Allen, T.H.; Morales, L.A. Reaction of Plutonium Dioxide with Water: Formation and Properties of PuO_{2+x}. *Science* **2000**, *287*, 285–287. [[CrossRef](#)] [[PubMed](#)]
2. Skomurski, F.; Shuller-Nickles, L.; Ewing, R.C.; Becker, U. Corrosion of UO₂ and ThO₂: A quantum-mechanical investigation. *J. Nucl. Mater.* **2008**, *375*, 290–310. [[CrossRef](#)]
3. Jonsson, M.; Nielsen, F.; Roth, O.; Ekeröth, E.; Nilsson, S.; Hossain, M.M. Radiation Induced Spent Nuclear Fuel Dissolution under Deep Repository Conditions. *Environ. Sci. Technol.* **2007**, *41*, 7087–7093. [[CrossRef](#)] [[PubMed](#)]
4. Cui, D.; Low, J.; Spahiu, K. Environmental behaviors of spent nuclear fuel and canister materials. *Energy Environ. Sci.* **2011**, *4*, 2537. [[CrossRef](#)]
5. Cotton, S. *Lanthanide and Actinide Chemistry*; Wiley: Hoboken, NJ, USA, 2006.
6. Morss, L.R.; Fuger, J.; Morss, L.R. *The Chemistry of the Actinide and Transactinide Elements*; Springer: Berlin/Heidelberg, Germany, 2006.
7. Dorado, B.; Amadon, B.; Freyss, M.; Bertolus, M. DFT+U calculations of the ground state and metastable states of uranium dioxide. *Phys. Rev. B* **2009**, *79*, 235125. [[CrossRef](#)]
8. Jomard, G.; Amadon, B.; Bottin, F.; Torrent, M. Structural, thermodynamic, and electronic properties of plutonium oxides from first principles. *Phys. Rev. B* **2008**, *78*, 075125. [[CrossRef](#)]
9. Cococcioni, M.; de Gironcoli, S. Linear response approach to the calculation of the effective interaction parameters in the LDA+U method. *Phys. Rev. B* **2005**, *71*, 035105. [[CrossRef](#)]
10. Anisimov, V.I.; Zaanen, J.; Andersen, O.K. Band Theory and Mott Insulators: Hubbard U instead of Stoner I. *Phys. Rev. B* **1991**, *44*, 943. [[CrossRef](#)] [[PubMed](#)]
11. Himmetoglu, B.; Floris, A.; de Gironcoli, S.; Cococcioni, M. Hubbard-corrected DFT energy functionals: The LDA+U description of correlated systems. *Int. J. Quant. Chem.* **2013**, *114*, 14–49. [[CrossRef](#)]

12. Dorado, B.; Garcia, P.; Carlot, G.; Davoisne, C.; Fraczekiewicz, M.; Pasquet, B.; Freyss, M.; Valot, C.; Baldinozzi, G.; Simeone, D.; et al. First-principles calculation and experimental study of oxygen diffusion in uranium dioxide. *Phys. Rev. B* **2011**, *83*, 035126. [[CrossRef](#)]
13. Liu, X.-Y.; Andersson, D.; Uberuaga, B.P. First-principles DFT modeling of nuclear fuel materials. *J. Mater. Sci.* **2012**, *47*, 7367–7384. [[CrossRef](#)]
14. Dorado, B.; Freyss, M.; Amadon, B.; Bertolus, M.; Jomard, G.; Garcia, P. Advances in first-principles modelling of point defects in UO₂: F electron correlations and the issue of local energy minima. *J. Phys. Condens. Matter* **2013**, *25*, 333201. [[CrossRef](#)] [[PubMed](#)]
15. Andersson, D.; Lezama, J.; Uberuaga, B.P.; Deo, C.; Conradson, S.D. Cooperativity among defect sites in AO_{2+x} and A₄O₉ (A = U, Np, Pu): Density functional calculations. *Phys. Rev. B* **2009**, *79*, 024110. [[CrossRef](#)]
16. Yu, J.; Devanathan, R.; Weber, W.J. First-principles study of defects and phase transition in UO₂. *J. Phys. Condens. Matter* **2009**, *21*, 435401. [[CrossRef](#)] [[PubMed](#)]
17. Dorado, B.; Jomard, G.; Freyss, M.; Bertolus, M. Stability of oxygen point defects in UO₂ by first-principles DFT+U calculations: Occupation matrix control and Jahn-Teller distortion. *Phys. Rev. B* **2010**, *82*, 035114. [[CrossRef](#)]
18. Allen, J.; Watson, G.W. Occupation matrix control of d- and f-electron localisations using DFT + U. *Phys. Chem. Chem. Phys.* **2014**, *16*, 21016–21031. [[CrossRef](#)]
19. Meredig, B.; Thompson, A.; Hansen, H.A.; Wolverton, C.; van de Walle, A. Method for locating low-energy solutions within DFT+U. *Phys. Rev. B* **2010**, *82*, 195128. [[CrossRef](#)]
20. Rabone, J.; Krack, M. A procedure for bypassing metastable states in local basis set DFT+U calculations and its application to uranium dioxide surfaces. *Comput. Mater. Sci.* **2013**, *71*, 157–164. [[CrossRef](#)]
21. Prodan, I.D.; Scuseria, G.E.; Martin, R.L. Covalency in the actinide dioxides: Systematic study of the electronic properties using screened hybrid density functional theory. *Phys. Rev. B* **2007**, *76*, 033101. [[CrossRef](#)]
22. Bo, T.; Lan, J.-H.; Zhao, Y.; Zhang, Y.-J.; He, C.; Chai, Z.; Shi, W.-Q. First-principles study of water adsorption and dissociation on the UO₂ (1 1 1), (1 1 0) and (1 0 0) surfaces. *J. Nucl. Mater.* **2014**, *454*, 446–454. [[CrossRef](#)]
23. Muggelberg, C.; Castell, M.; Briggs, G.; Goddard, D. An STM study of the UO₂(001) surface. *Appl. Surf. Sci.* **1999**, *142*, 124–128. [[CrossRef](#)]
24. Taylor, T.; Ellis, W. Distorted surface oxygen structure on UO₂ (100). *Surf. Sci.* **1981**, *107*, 249–262. [[CrossRef](#)]
25. Tasker, P.W. The structure and properties of fluorite crystal surfaces. *J. Phys. Colloq.* **1980**, *41*, 6. [[CrossRef](#)]
26. Chatzimichail, R.; Bebelis, S.; Nikolopoulos, P. Temperature Dependence of the Surface Energy of the Low Index Planes of UO₂ and ThO₂. *J. Mater. Eng. Perform.* **2016**, *25*, 1691–1696. [[CrossRef](#)]
27. Abramowski, M.; Redfern, S.; Grimes, R.; Owens, S. Modification of UO₂ crystal morphologies through hydroxylation. *Surf. Sci.* **2001**, *490*, 415–420. [[CrossRef](#)]
28. Jomard, G.; Bottin, F. Thermodynamic stability of PuO₂ surfaces: Influence of electronic correlations. *Phys. Rev. B* **2011**, *84*, 195469. [[CrossRef](#)]
29. Tan, A.H.; Grimes, R.W.; Owens, S. Structures of UO₂ and PuO₂ surfaces with hydroxide coverage. *J. Nucl. Mater.* **2005**, *344*, 13–16. [[CrossRef](#)]
30. Jelea, A.; Colbert, M.; Ribeiro, F.; Tréglia, G.; Pellenq, R.-M. An atomistic modelling of the porosity impact on UO₂ matrix macroscopic properties. *J. Nucl. Mater.* **2011**, *415*, 210–216. [[CrossRef](#)]
31. Sattonnay, G.; Tétot, R. Bulk, surface, and point defect properties in UO₂ from a tight-binding variable-charge model. *J. Phys. Condens. Matter* **2013**, *25*, 125403. [[CrossRef](#)]
32. Benson, G.C.; Freeman, P.J.; Dempsey, E. Calculation of Cohesive and Surface Energies of Thorium and Uranium Dioxides. *J. Am. Ceram. Soc.* **1963**, *46*, 43–47. [[CrossRef](#)]
33. Boyarchenkov, A.; Potashnikov, S.; Nekrasov, K.; Kupryazhkin, A. Molecular dynamics simulation of UO₂ nanocrystals surface. *J. Nucl. Mater.* **2012**, *421*, 1–8. [[CrossRef](#)]
34. Wul, G. Zur Frage der Geschwindigkeit des Wachstums und der Auflösung der Kristalle. *Z. Kristallogr.* **1901**, *34*, 449–530.
35. Wang, G.; Batista, E.R.; Yang, P. Ligand induced shape transformation of thorium dioxide nanocrystals. *Phys. Chem. Chem. Phys.* **2018**, *20*, 17563–17573. [[CrossRef](#)] [[PubMed](#)]
36. Moxon, S.; Symington, A.R.; Tse, J.S.; Dawson, J.; Flitcroft, J.M.; Parker, S.C.; Cooke, D.J.; Harker, R.M.; Molinari, M. The energetics of carbonated PuO₂ surfaces affects nanoparticle morphology: A DFT+U study. *Phys. Chem. Chem. Phys.* **2020**. [[CrossRef](#)] [[PubMed](#)]

37. Rák, Z.; Ewing, R.C.; Becker, U. Hydroxylation-induced surface stability of AnO₂ (An=U, Np, Pu) from first principles. *Surf. Sci.* **2013**, *608*, 180–187. [[CrossRef](#)]
38. Alexandrov, V.; Shvareva, T.Y.; Hayun, S.; Asta, M.; Navrotsky, A. Actinide Dioxides in Water: Interactions at the Interface. *J. Phys. Chem. Lett.* **2011**, *2*, 3130–3134. [[CrossRef](#)]
39. Shields, A.E.; Santos-Carballal, D.; de Leeuw, N.H. A density functional theory study of uranium-doped thorium and uranium adatoms on the major surfaces of thorium dioxide. *J. Nucl. Mater.* **2016**, *473*, 99–111. [[CrossRef](#)]
40. Evarestov, R.A.; Bandura, A.V.; Blokhin, E. Surface modelling on heavy atom crystalline compounds: HfO₂ and UO₂ fluorite structures. *Acta Mater.* **2009**, *57*, 600–606. [[CrossRef](#)]
41. Chaka, A.M.; Oxford, G.A.; Stubbs, J.E.; Eng, P.J.; Bargar, J.R. Density-functional theory investigation of oxidative corrosion of UO₂. *Comput. Theor. Chem.* **2012**, *987*, 90–102. [[CrossRef](#)]
42. Weck, P.F.; Jove-Colon, C.F.; Sassani, D.C.; Kim, E. On the role of strong electron correlations in the surface properties and chemistry of uranium dioxide. *Dalton Trans.* **2013**, *42*, 4570. [[CrossRef](#)]
43. Bottin, F.; Geneste, G.; Jomard, G. Thermodynamic stability of the UO₂ surfaces: Interplay between over-stoichiometry and polarity compensation. *Phys. Rev. B* **2016**, *93*, 115438. [[CrossRef](#)]
44. Sun, B.; Liu, H.; Song, H.; Zhang, G.; Zheng, H.; Zhao, X.; Zhang, P. First-principles study of surface properties of PuO₂: Effects of thickness and O-vacancy on surface stability and chemical activity. *J. Nucl. Mater.* **2012**, *426*, 139–147. [[CrossRef](#)]
45. Senanayake, S.D.; Waterhouse, G.I.N.; Chan, A.; Madey, T.; Mullins, D.; Idriss, H. The reactions of water vapour on the surfaces of stoichiometric and reduced uranium dioxide: A high resolution XPS study. *Catal. Today* **2007**, *120*, 151–157. [[CrossRef](#)]
46. Senanayake, S.D.; Waterhouse, G.I.N.; Chan, A.S.Y.; Madey, T.E.; Mullins, D.R.; Idriss, H. Probing Surface Oxidation of Reduced Uranium Dioxide Thin Film Using Synchrotron Radiation. *J. Phys. Chem. C* **2007**, *111*, 7963–7970. [[CrossRef](#)]
47. Ganduglia-Pirovano, M.V.; da Silva, J.L.F.; Sauer, J. Density-Functional Calculations of the Structure of Near-Surface Oxygen Vacancies and Electron Localization on CeO₂(111). *Phys. Rev. Lett.* **2009**, *102*, 026101. [[CrossRef](#)] [[PubMed](#)]
48. Calaza, F.C.; Xu, Y.; Mullins, D.R.; Overbury, S.H. Oxygen Vacancy-Assisted Coupling and Enolization of Acetaldehyde on CeO₂(111). *J. Am. Chem. Soc.* **2012**, *134*, 18034–18045. [[CrossRef](#)]
49. Idriss, H. Surface reactions of uranium oxide powder, thin films, and single crystals. *Surf. Sci. Rep.* **2010**, *65*, 67–109. [[CrossRef](#)]
50. Schlereth, T.W.; Hedhili, M.N.; Yakshinskiy, B.V.; Gouder, T.; Madey, T.E. Adsorption and Reaction of SO₂ with a Polycrystalline UO₂ Film: Promotion of S–O Bond Cleavage by Creation of O-Defects and Na or Ca Coadsorption. *J. Phys. Chem. B* **2005**, *109*, 20895–20905. [[CrossRef](#)]
51. Manner, W.L.; Lloyd, J.A.; Paffett, M.T. Reexamination of the fundamental interactions of water with uranium. *J. Nucl. Mater.* **1999**, *275*, 37–46. [[CrossRef](#)]
52. Konno, H. *X-ray Photoelectron Spectroscopy, in Materials Science and Engineering of Carbon*; Elsevier: Amsterdam, The Netherlands, 2016; pp. 153–171.
53. Wellington, J.P. Oxygen Vacancy Formation and Water Adsorption on Reduced AnO₂ {111}, {110}, and {100} Surfaces (An = U, Pu): A Computational Study. *J. Phys. Chem. C* **2018**, *122*, 7149–7165. [[CrossRef](#)]
54. Bo, T.; Lan, J.-H.; Wang, C.-Z.; Zhao, Y.; He, C.-H.; Zhang, Y.-J.; Chai, Z.-F.; Shi, W.-Q. First-Principles Study of Water Reaction and H₂ Formation on UO₂ (111) and (110) Single Crystal Surfaces. *J. Phys. Chem. C* **2014**, *118*, 21935–21944. [[CrossRef](#)]
55. Wang, G.; Batista, E.R.; Yang, P. Excess Electrons on Reduced AnO₂ (111) Surfaces (An = Th, U, Pu) and Their Impacts on Catalytic Water Splitting. *J. Phys. Chem. C* **2019**, *123*, 30245–30251. [[CrossRef](#)]
56. Chen, J.-L.; Kaltsoyannis, N. Computational Study of the Bulk and Surface Properties of the Minor Actinide Dioxides MAnO₂ (Man = Np, Am, Cm); Water Adsorption on Stoichiometric and Reduced {111}, {110} and {100} Surfaces. *J. Phys. Chem. C* **2019**, 15540–15550. [[CrossRef](#)]
57. Li, H.-Y.; Wang, H.-F.; Gong, X.-Q.; Guo, Y.-L.; Guo, Y.; Lu, G.; Hu, P. Multiple configurations of the two excess 4f electrons on defective CeO₂(111): Origin and implications. *Phys. Rev. B* **2009**, *79*, 193401. [[CrossRef](#)]
58. Senanayake, S.D.; Idriss, H. Water reactions over stoichiometric and reduced UO₂ (111) single crystal surfaces. *Surf. Sci.* **2004**, *563*, 135–144. [[CrossRef](#)]

59. Senanayake, S.D.; Rousseau, R.; Colegrave, D.; Idriss, H. The reaction of water on polycrystalline UO₂: Pathways to surface and bulk oxidation. *J. Nucl. Mater.* **2005**, *342*, 179–187. [[CrossRef](#)]
60. Seibert, A.; Gouder, T.; Huber, F. Interaction of PuO₂ thin films with water. *Radiochim. Acta* **2010**, *98*, 647–657. [[CrossRef](#)]
61. Gouder, T.; Shick, A.; Huber, F. Surface Interaction of PuO₂, UO_{2+x} and UO₃ with Water Ice. *Top. Catal.* **2013**, *56*, 1112–1120. [[CrossRef](#)]
62. Haschke, J.M.; Allen, T.H.; Morales, L.A. Reactions of plutonium dioxide with water and hydrogen–oxygen mixtures: Mechanisms for corrosion of uranium and plutonium. *J. Alloy. Compd.* **2001**, *314*, 78–91. [[CrossRef](#)]
63. Haschke, J.M.; Ricketts, T.E. Adsorption of water on plutonium dioxide. *J. Alloy. Compd.* **1997**, *252*, 148–156. [[CrossRef](#)]
64. Tian, X.-F.; Wang, H.; Xiao, H.; Gao, T. Adsorption of water on UO₂ (111) surface: Density functional theory calculations. *Comput. Mater. Sci.* **2014**, *91*, 364–371. [[CrossRef](#)]
65. Zhang, L.; Sun, B.; Zhang, Q.; Liu, H.; Liu, K.; Song, H. Polaron modulation mechanism of H₂O and CO₂ adsorption on PuO₂ (111) surface. *Appl. Surf. Sci.* **2020**, 146164. [[CrossRef](#)]
66. Wellington, J.P.; Kerridge, A.; Austin, J.; Kaltsoyannis, N. Electronic structure of bulk AnO₂ (An = U, Np, Pu) and water adsorption on the (111) and (110) surfaces of UO₂ and PuO₂ from hybrid density functional theory within the periodic electrostatic embedded cluster method. *J. Nucl. Mater.* **2016**, *482*, 124–134. [[CrossRef](#)]
67. Tegner, B.E.; Molinari, M.; Kerridge, A.; Parker, S.C.; Kaltsoyannis, N. Water adsorption on AnO₂ {111}, {110}, and {100} surfaces (An = U and Pu): A density functional theory+ U study. *J. Phys. Chem. C* **2017**, *121*, 1675–1682. [[CrossRef](#)]
68. Tegner, B.E.; Kaltsoyannis, N. Multiple water layers on AnO₂ {111}, {110}, and {100} surfaces (An = U, Pu): A computational study. *J. Vacuum Sci. Technol. A Vacuum Surf. Films* **2018**, *36*, 041402. [[CrossRef](#)]
69. Maldonado, P.; Evins, L.Z.; Oppeneer, P.M. Ab Initio Atomistic Thermodynamics of Water Reacting with Uranium Dioxide Surfaces. *J. Phys. Chem. C* **2014**, *118*, 8491–8500. [[CrossRef](#)]
70. Zhang, C.; Yang, Y.; Zhang, P. Dissociation Mechanism of Water Molecules on the PuO₂(110) Surface: An Ab Initio Molecular Dynamics Study. *J. Phys. Chem. C* **2017**, *122*, 371–376. [[CrossRef](#)]
71. Carlson, R.K.; Cawkwell, M.J.; Batista, E.R.; Yang, P. Tight-Binding Modeling of Uranium in an Aqueous Environment. *J. Chem. Theory Comput.* **2020**, *16*, 3073–3083. [[CrossRef](#)] [[PubMed](#)]



© 2020 by the authors. Licensee MDPI, Basel, Switzerland. This article is an open access article distributed under the terms and conditions of the Creative Commons Attribution (CC BY) license (<http://creativecommons.org/licenses/by/4.0/>).